Journal of the Mechanical Behavior of Biomedical Materials 98 (2019) 121–130

Contents lists available at ScienceDirect

Journal of the Mechanical Behavior of Biomedical Materials

journal homepage: www.elsevier.com/locate/jmbbm

Response of mechanically-created neurites to extension

Madeleine Anthonisen[a,*], Matthew Rigby[a], M. Hussain Sangji[b], Xue Ying Chua[a], Peter Grütter[a]

[a] Department of Physics, McGill University, 3600 Rue University, Montréal, Québec, H3A2T8, Canada
[b] Department of Biomedical Engineering, Northwestern University, 3600 Rue University, Montréal, Québec, H3A2T8, Canada

ARTICLE INFO

Keywords:
Uniaxial strain
Mechanical properties
Pipette micromanipulation
Axonal growth
Rat hippocampus

ABSTRACT

We use micromanipulation techniques and real-time particle tracking to develop an approach to study specific attributes of neuron mechanics. We use a mechanical probe composed of a hollow micropipette with its tip fixed to a functionalized bead to induce the formation of a neurite in a sample of rat hippocampal neurons. We then move the sample relative to the pipette tip, elongating the neurite while simultaneously measuring its tension by optically tracking the deflection of the beaded tip. By calibrating the spring constant of the pipette, we can convert this deflection to a force. We use this technique to obtain uniaxial strain measurements of induced neurites and investigate the dependence of the force-extension relationship on mechanical pull speed. We show that in the range of pull speeds studied (0.05–1.8 μm/s), the variation in the work to extend a neurite 10 μm is consistent across pull speeds. We do not observe statistically significant rate-dependent effects in the force-extension profiles; instead we find the same quadratic behaviour (with parameters drawn from the same distributions) at each pull speed.

1. Introduction

Tension is a fundamental driver of neurite growth and development [O'Toole et al. (2008); Athamneh and Suter (2015)]. This has been demonstrated by a series of experiments in which mechanical tension, applied with microneedles, is used to initiate and elongate axons (see e.g. [Bray (1984); Dennerll et al. (1989); Lamoureux et al. (2002); Bernal et al. (2007); O'Toole et al. (2008); Magdesian et al. (2016)]). In all types of axons investigated (embryonic chick sensory [Zheng et al. (1991)], rat hippocampal [Lamoureux et al. (2002)], and rat ganglion [Steketee et al. (2014)]) elongation rate was found to depend linearly on tension applied. This is evidence of a connection between tension and the axonal assembly process [O'Toole et al. (2008); Athamneh and Suter (2015)]. The surprisingly rapid addition of new cellular material during neurite elongation as well as the exact mechanisms and the limits by which tension influences this mass accretion present many open questions [Athamneh and Suter (2015); Heidemann and Bray (2015)] such as whether the stimulus governing mechanotransduction is force or deformation.

We present a methodology based on micromanipulation tools and particle-tracking techniques to measure neurite mechanics. In [Lucido et al. (2009)] it is shown that when polystyrene beads coated with positively-charged poly-D-lysine (PDL) contact axons or dendrites, presynaptic structures form, which adhere to the bead. If this bead is then pulled, the growth of an auxiliary structure, the neurite, is induced. In [Magdesian et al. (2016)], micropipettes, suction and PDL-coated beads were combined to exploit the advantages of each as micromanipulation tools to create *de novo* functional neurites. These neurites contained cytoskeleton elements and could transmit electrical signals. Here, we extend the work in [Magdesian et al. (2016)] by performing force measurements on individual neurites as they are being pulled. This is achieved by fabricating mechanically compliant micropipettes, suitably calibrating their spring constants and applying particle-tracking techniques to determine force-elongation relationships of neurites being pulled. This gives us qualitative and quantitative information on the relationship between elongation and the force involved which can ultimately be used to extract material parameters for neurites and to model neurite growth. The controlled release of neurite-tethered beads, rendered possible by suction, opens the door to complex neuronal re-wiring experiments [Magdesian et al. (2016); Rigby et al. (2019)]. This is an advantage over other techniques used to quantify forces in axons and dendrites, such as those that employ just microneedles or atomic force microscopy (AFM) [Franze et al. (2009); Karhu et al. (2009); Fuhs et al. (2013); Athamneh et al. (2015)].

In the following, we measure force-extension relationships for a range of extension rates. Previous work done with the same method at rates of ~ 0.025 μm/s [Magdesian et al. (2016)] and ~ 0.5 μm/s [Suarez et al. (2013)] reports the formation of neurites containing the same

* Corresponding author.
E-mail address: madeleine.anthonisen@mail.mcgill.ca (M. Anthonisen).

https://doi.org/10.1016/j.jmbbm.2019.06.015
Received 9 February 2019; Received in revised form 24 May 2019; Accepted 17 June 2019
Available online 19 June 2019
1751-6161/

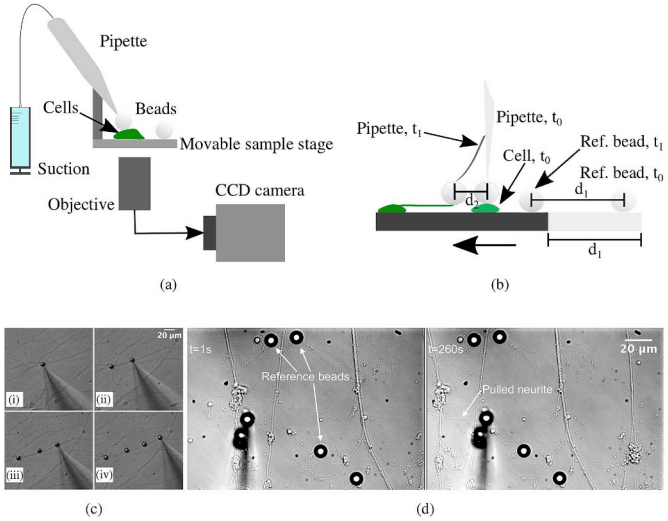

Fig. 1. (a) Schematic of set-up for the initiation, elongation and detection of tension of neurites. The sample cells are mounted on a piezo-actuated nano positioning stage that is controlled by a CPU. A micropipette held in a micromanipulator approaches the sample from above the stage. The back of the pipette is connected to a 1 ml syringe via plastic tubing which allows for the controlled pick-up and release of beads. The sample is contacted optically from below by the 40× objective of an inverted optical microscope connected to a CCD camera which captures 512×512 pixel images. **(b)** Schematic of a pull (side view). At t_1, the stage has been moved to the left by d_1. The pipette bends by an amount d_2. The length the neurite has been pulled at t_1 is $d_1 - d_2$. **(c)** Demonstration of the capacity to control the adhesion sites of functionalized beads using suction. **(d)** Initiation and elongation of a neurite with a 10 μm PDL-coated bead and pipette micromanipulations. Snapshots depicting a neurite being pulled (arrow) by keeping the micropipette and the bead stationary and moving the stage (left in this instance). Reference beads are also indicated (arrows). Images are acquired at a rate of 1 Hz.

proteins as axons (including actin and tubulin). However, these papers made no attempt at quantifying the force-extension relationship involved. In this paper, we explore this relation in the regime between these two bounds. We pull at speeds up to 1.8 μm/s; to our knowledge this is 18 times faster than the fastest speeds ever reported in axon pulling experiments [Pfister et al. (2004)] and over 300 times faster than the fastest *in vivo* growth rates for axons of the same type [Dotti et al. (1988); Waxman et al. (1995)]. Surprisingly, we do not observe rate-dependent behaviour over a 10-fold increase in speed. We observe the variation in the fit parameters describing the force extension profiles to be the same across all pull speeds investigated.

2. Materials and methods

2.1. Experimental set-up

The apparatus contains five main elements, which are described below. Throughout the description, we refer to Fig. 1a, which shows a schematic representation of the apparatus that features only the main components. These components are:

1 The neuron: Rat hippocampal neurons are cultured on coverslips and mounted in a fluid cell.
2 Movable platform: The fluid cell is fixed to a movable platform. The platform is a computer-controlled piezo stage constrained to move in two dimensions with a 90 μm×90 μm range.
3 A pipette: A pipette is held in a fixed location; it is prepared so that one of its ends is tapered. The tapered end is flexible; this flexibility is important, as it will be used to measure the force exerted by the neurite. Suction is applied through the pipette by means of a syringe attached to the back-end of the pipette. The suction is used to hold a microbead firmly to the tapered end. This allows the controlled release of beads, demonstrated in Fig. 1c, which is an advantage compared to AFM.
4 A microbead: Microbeads coated with PDL are randomly distributed in the medium in which the neurons grow. When a microbead makes contact with a neuron, the PDL coating stimulates the formation of a synapse and thus a stable mechanical contact [Suarez et al. (2013)]. This connection is sufficiently strong as to withstand all manipulations imposed upon it during the experiment.
5 A microscope/camera: An inverted optical microscope (Olympus 71-X equipped with a 40× objective, NA = 0.6), and a CCD camera (Cascade II, Photometrics) are used to acquire optical microscope images at rates of 1 Hz and 5.5 Hz.

To initiate and elongate a neurite, a bead-tipped pipette contacts a neuron for 30 min so a synapse can form (see Fig. 1b and d) [Lucido et al. (2009); Magdesian et al. (2016)]. Most of the data presented in the Results and Discussion section is obtained with beads fixed to the pipette tips with glue instead of with suction. This is to avoid potential errors in the displacement measurements due to small movements of the bead relative to the pipette tip as tension is applied. The sample stage is moved relative to the beaded pipette tip, thus applying a force on the neuron; the result is the mechanical creation and elongation of a new neurite. The mechanism allows the neurite to be pulled over large distances (>80 μm) at very high rates (we report pull speeds up to 1.8 μm/s).

In our experiments, we use a Sutter Pipette Puller (Flaming/Brown, model P-87) to fabricate pipettes with spring constants ~ 0.001 N/m and track the beaded tip with a resolution of ~ 20 nm. This provides a force measurement with resolution ~ 0.02 nN.

2.2. Bead tracking

As the neurite is pulled, we acquire microscope images and optically track the positions of all the beads in these images with a custom-made centroid-tracking algorithm [Cheezum et al. (2001)]. We track beads fixed to the sample surface, termed “reference beads”, to obtain the distance the platform has been moved ($d_1(t)$ in Fig. 1b). We also track the bead at the pipette tip to obtain the deflection of the pipette (this is $d_2(t)$ in Fig. 1b). The value of $d_1(t) - d_2(t)$ corresponds to the length the neurite is extended at time $t > t_0$, where t_0 is the time the platform is set in motion.

To characterize the stability and noise of our system, we measure the displacements over time of reference beads without moving the sample stage. Typical profiles of these displacements are shown in Fig. 2a, while Fig. 2b shows normal distributions that are fitted to these displacements. We find the displacement of an individual bead has a stable and constant mean for extended periods of time with a standard deviation of ~ 20 nm, dominated by bead-tracking error. Averaging the displacements of several beads in the same image series reduces this error to ~ 10 nm. In the following, we take the error in bead displacement, δd_i, to be 20 nm. The accuracy of the tracking algorithm was investigated by using computer-generated data that simulated measurements of bead locations, and then comparing the measurements produced by the tracking mechanism with the known “locations” in the data. The error was approximately 4 percent of a pixel, which is 16 nm. Other work has shown the variance of the lateral motion estimation is

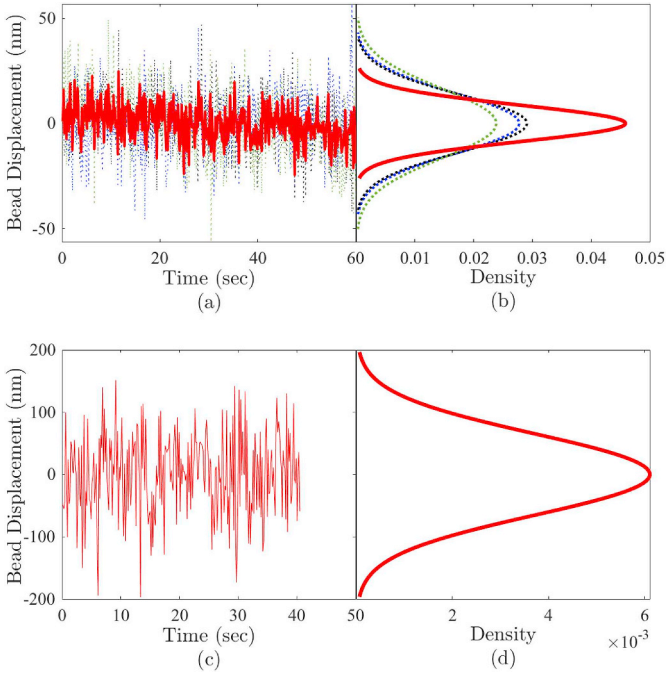

Fig. 2. (a–b) Tracking of beads fixed to the fluid cell surface with the stage kept stationary. Dashed lines are individual bead displacements and the average of the individual time series is in red. **(a)** The displacement of beads versus time, images acquired at a 5.5 Hz rate. **(b)** Normal distributions of displacements. The distribution of the average of the individual time series in **(a)** has a standard deviation of ~10 nm. **(c–d)** Tracking of a bead fixed to the tip of a pipette with stiffness 0.001 N/m. The pipette was held stationary while the sample stage was moved (a null experiment). **(c)** The displacement of the tip-bead versus time. **(d)** The distribution of displacement has a standard deviation of ~65 nm. (For interpretation of the references to colour in this figure legend, the reader is referred to the Web version of this article.)

proportional to the square of the sampling width and inversely proportional to the average signal-to-noise ratio [Zhang and Menq (2008); Alexander and Ng (1991); Ares and Arines (2004)]. Therefore, sub-nanometer bead motion could be measured by reducing the sampling width (e.g. with higher magnification and a camera with smaller pixels) and by increasing the signal-to-noise ratio by increasing the illumination intensity. Note that neurons are photo-sensitive so optical power should be minimized. However, as we will show, our tracking sensitivity is more than adequate to observe neuron mechanics.

To ensure an accurate interpretation of biological measurements, several "null" experiments are performed by moving the sample stage (without neurons) and tracking the tip-bead, Fig. 2c and d. This allows us to determine the force-noise in our measurements due to mechanical vibrations coupling to the instrument. The distribution of the displacement of the tip-bead has a standard deviation of ~65 nm.

2.3. Probe preparation and calibration

Flexible micropipettes with tip outer diameters of 0.5–2 μm were manufactured by locally heating the centers of glass capillary tubes (1.5 mm outer diameter, King Precision Glass Inc) and rapidly pulling the two ends apart in a Sutter Pipette Puller (Flaming/Brown, model P-87). Both pull speed and temperature influence pipette geometry, and these are chosen so as to obtain flexible micropipettes with long tapers (~5 mm, see Fig. 3a) [Shimamoto and Kapoor (2012)]. We calibrate the pipette stiffness with standard AFM measurements following the procedure outlined in [Shimamoto and Kapoor (2012); Hutter (2005)], wherein the spring constant is obtained by comparison to a reference probe of known stiffness. Using the MFP-3D-BIO AFM (Asylum Instruments), we calibrated a commercial AFM cantilever (HQ:CSC38, μmasch) according to the thermal noise method [Hutter and Bechhoefer (1993)]. This "reference" cantilever was then used to collect force-distance curves at the pipette tip (see Fig. 3). For each pipette, several force-distance curves were acquired and the mean and standard deviation of probe stiffness were computed. Spring constants of pipettes

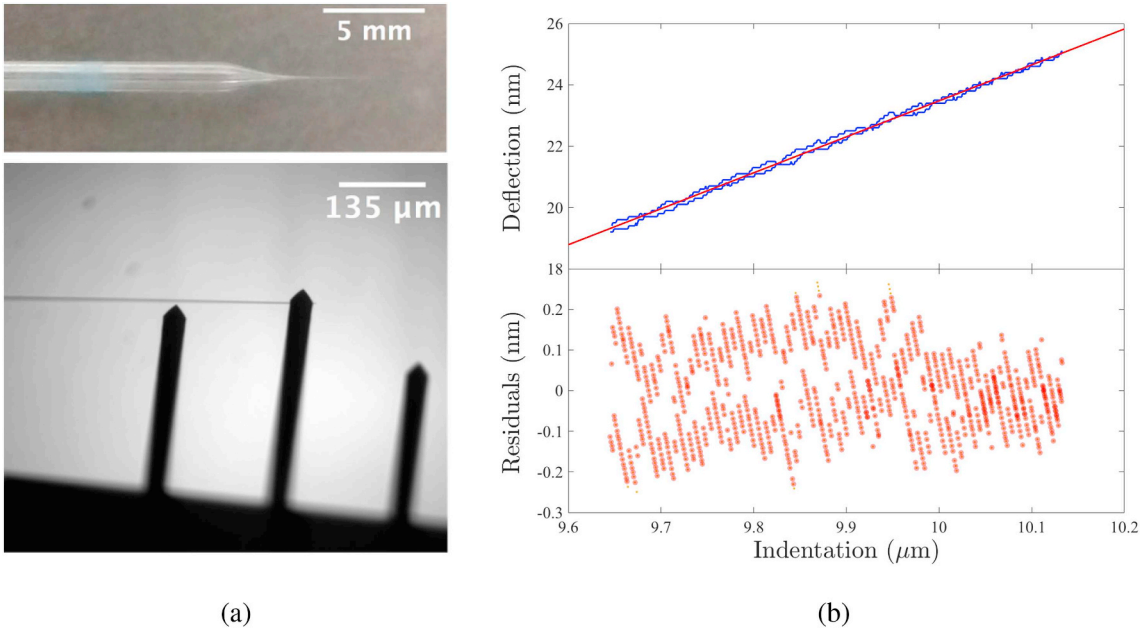

Fig. 3. Calibration of a micropipette with a reference cantilever. **(a)** Top: Micropipette with a long taper. Bottom: Image of an AFM cantilever, spring constant of 0.0483 N/m, contacting a micropipette. **(b)** Upper graph is the linear region of a force-distance curve acquired on a micropipette. The two blue lines are the indentation and retraction curves. The inverse slope of the linear fit (red line) is used to obtain the micropipette stiffness. The fit residuals are plotted below. (For interpretation of the references to colour in this figure legend, the reader is referred to the Web version of this article.)

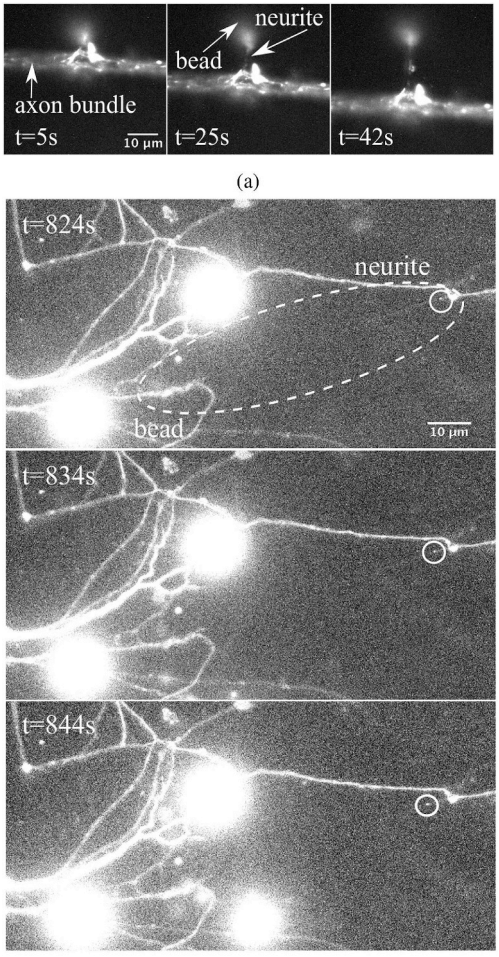

Fig. 4. Cytoskeleton elements in newly-created neurites. **(a)** A neurite pulled from an axon bundle expressing actin-GFP (at a speed of $\sim 0.5\,\mu$m/s) is observed to fluoresce. From one still image to the next the stage has been moved down relative to the stationary bead. **(b)** Microtubule growth marked by fluorescent EB3-GFP (white circles) in a newly-created neurite (pulled for $\sim 87\,\mu$m at an average rate of $0.2\,\mu$m/s).

used to measure force-extension curves range from $(1.0 \pm 0.1) \times 10^{-3}$ to $(1.6 \pm 0.2) \times 10^{-2}$ N/m. Note that increasing the opening of the pipette tip (e.g. by pulling at a slower rate and/or at a lower temperature) leads to a stiffer probe that applies suction to beads more easily. We find pipettes with stiffnesses ~0.01–0.02 N/m can easily manipulate beads (see Fig. 1c) while maintaining the flexibility necessary to observe forces in neurites. Typically, commercially available cantilevers designated for biological experiments have minimal spring constants of 0.01 N/m whereas micropipettes can be made an order of magnitude more compliant.

2.4. Neuronal cultures

All procedures were approved by McGill University's Animal Care Committee and conformed to the guidelines of the Canadian Council of Animal Care. Following the procedures outlined in [Magdesian et al. (2017); Lucido et al. (2009)] and references therein, hippocampal neurons from Sprague Dawley rat embryos (either sex) were isolated and placed on 25 mm glass coverslips (Warner Instruments) coated with 100 μg/ml PDL (Sigma-Aldrich). Samples were immersed in Neurobasal Medium (Life Technologies) supplemented with serum-free B-27 (volume ratio 1:50) and penicillin/streptomycin/glutamine (volume ratio 1:10) and maintained in the incubator (37°C, 5 %CO_2) for 7–21 days before measurements. Experiments were performed at room temperature and cells were continuously perfused with oxygen-infused physiological saline solution [consisting of 135 mM NaCl (Sigma-Aldrich), 3.5 mM KCl (Sigma-Aldrich), 2 mM $CaCl_2$ (Sigma-Aldrich), 1.3 mM $MgCl_2$ (BDH), 10 mM HEPES (ThermoFisher Scientific), 20 mM D-glucose (Invitrogen) [Magdesian et al. (2017)]. To regulate the cell environment, pH was maintained between 7.3 and 7.4 and osmolarity between 240 and 260 mOsm. Data presented in this work is from 19 dishes, each with a cell density of $\sim 10^6$ neurons/mL.

2.4.1. Immunocytochemistry and properties of pulled neurites

Evidence that the pulled structures created with beads are in fact neurites makes this work relevant to questions of axonal growth. In this subsection, we address the question "are we pulling neurites?" by performing fluorescent microscopy to identify two cytoskeleton elements, actin and microtubules, in newly-created neurites. We also discuss references that give further evidence that our structures are axon-like.

Fig. 4a shows actin present in an extension pulled at a speed of $0.5\,\mu$m/s from an axon bundle expressing actin-GFP. The live-cell fluorogenic F-actin labeling probe (100 nM) was added to 2 ml of the physiological saline solution and incubated for 6 h after which the medium containing the probe was replaced with new physiological saline.

In Fig. 4b, microtubule growth is captured with a fluorescently-tagged end-binding (EB) protein, End-Binding Protein 3-Green Fluorescent Protein (EB3-GFP). EB proteins are a type of Microtubule Associated Protein that bind to the ends of microtubules so when fluorescently tagged, they are markers of microtubule growth. In Fig. 4b, variations in intensity along the neurite show microtubules growing towards the distal end of the neurite $\sim$ 824 seconds after its creation, the earliest time fluorescent recordings were acquired. Cell lines expressing fluorescently-labelled EB3 were prepared by viral transfection. Lentiviruses were a gift from the Fournier lab [Kaplan et al. (2017)]. Neurons were infected overnight with purified lentivirus at a multiplicity of infection (MOI) of 2–3.

Fluorescence microscopy was performed using a Zeiss Axiovert 200 M microscope and a 63× objective (Zeiss), with the fluorescent probes illuminated by a Xenon arc bulb (Sutter Instruments).

In previous works [Suarez et al. (2013); Sánchez (2011)], extensions were induced from axons expressing two other fluorescent proteins, one at a time: synaptophysin-GFP and bassoon-GFP, as well as from axons where the dye Tubulin Tracker™ Green (Invitrogen) was used to fluorescently label tubulin. In all cases, newly-created extensions (pulled at speeds $>0.5\,\mu$m/s) were observed to fluoresce, indicating these proteins are also present in the extensions.

We note that while it is uncertain that the proteins present are structured in a functional way at the timescales considered in this work [Magdesian et al. (2016)], showed that neurites induced by PDL-coated beads are electrically functional 24 h after creation. As in [Magdesian et al. (2016)], we allow the bead to contact the neuron for 30 min prior to pulling, long enough for a synapse to be induced. This increases the probability that we are pulling a neurite-like structure versus membrane tethers, which are cylindrical lipid structures that dynamically form on the cell membrane within seconds of being contacted by an

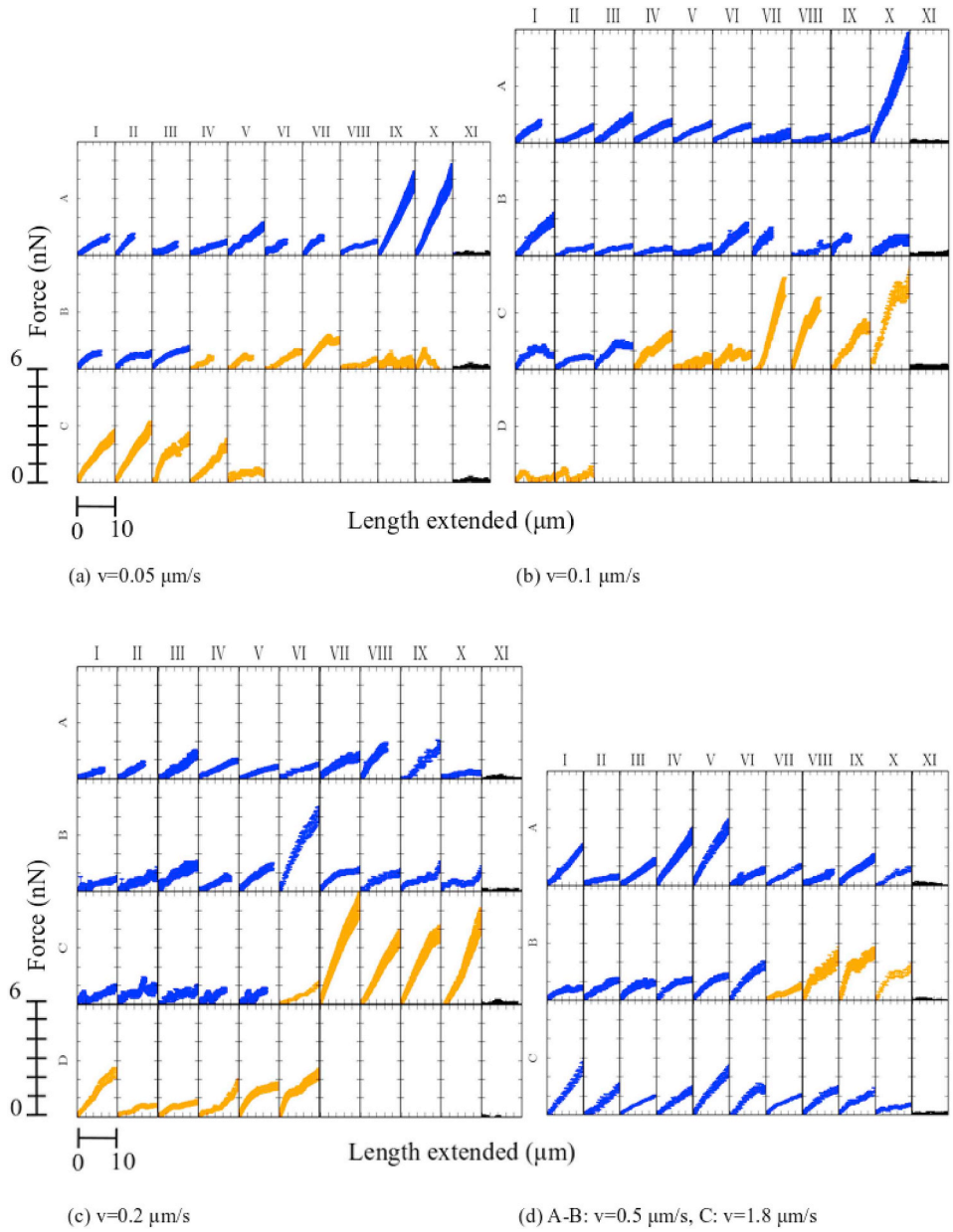

Fig. 5. Responses of rat hippocampal neurites to mechanical forces applied under different elongation rates. Each curve corresponds to a single pull inducing one or more neurites. Curves were obtained for pull speeds of 0.05 μm/s **(a)**, 0.1 μm/s **(b)**, 0.2 μm/s **(c)**, 0.5 μm/s **(d)**, rows A and B, and 1.8 μm/s **(d)**, row C. "Type I" curves are in blue, "type II" curves are in gold and null experiments (occupying the last columns of a-d) are in black. Calculation of error bars as described in text. (For interpretation of the references to colour in this figure legend, the reader is referred to the Web version of this article.)

adhesive bead [Hochmuth et al. (1996); Dai et al. (1998)]. The identifiable components of an axon are present in our extensions suggesting these have similar mechanical properties and will develop into functional neurites.

3. Results and Discussion

3.1. Uniaxial strain measurements

In the following, we apply our force-sensing pipette technique to investigate the mechanics of extending neurons. The details of the procedure to initiate and pull a neurite are described in [Magdesian et al. (2017)]. The flexible pipette method allows us to investigate the force-extension relationship of neurites over distances of 0–10 μm. Fig. 5 shows the force-extension relationships for pulls at 5 different extension rates, 5 to 300 times greater than the *in vivo* rates of the fastest growing neurons (0.006 μm/s to 0.01 μm/s [Dotti et al. (1988); Waxman et al. (1995)]). Inspection of Fig. 5 shows that the spread of neurite deformability is largely uniform across the regime of pull speeds considered. Error bars are from combining the error in pipette stiffness and the error in the displacement of the beaded tip with the error formula for products. Fig. 5c, curves C− VI and C− VII were measured with beads fixed to pipette tips using suction; in the other cases the beads were glued to the tips. An interesting question is if all the curves

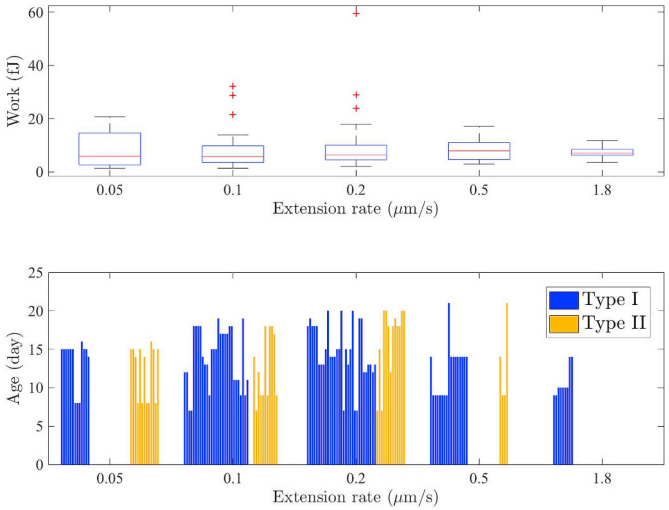

Fig. 6. Top: Box plot summarizing the data displayed in Fig. 5. For every curve in Fig. 5, a value of work was computed by summing the product of extension and corresponding force. These values are plotted here. For each box, the central line corresponds to the median work value with the top and bottom edges of the box indicating the 75th and 25th percentiles of the data respectively. The whiskers encompass the most extreme data points except for the outliers which are indicated by the red crosses. Comparisons of the groups show no statistical significance (p>0.1) according to the Kruskal-Wallis test. Bottom: Bar graph of the ages of cell cultures; bars are grouped according to extension rate and classification type. This shows age is not an important factor affecting deformability. (For interpretation of the references to colour in this figure legend, the reader is referred to the Web version of this article.)

are similar. By eye it seems that some curves are monotonic (for example Fig. 5a, curve A– X), whereas others have discontinuities (for example Fig. 5a, curve B– VII). We use a statistically robust approach to address this question in two steps. First, we test whether our data can support a dependence of the force-extension relationship on pull rate, and second, we categorize curves by type (monotonic or non-monotonic) and by the number of parameters needed to fit their functional dependence.

To determine if the pulling rate matters we compute the integral of each curve (i.e. the work to extend a neurite) and compare sets (grouped by pull speed) with the Kruskal-Wallis test. We use the Kruskal-Wallis test because it does not require samples to follow a normal distribution. This test reveals no significant statistical difference between sets, the scatter in each set is consistent for all pull speeds. These results are summarized in Fig. 6.

In Fig. 6, we also show the age of the neurites (days *in vitro*), grouped by pull speed and classification type (discussed below). Age and work to extend a neurite have a correlation coefficient of ~0.05, which indicates age is not an important factor affecting deformability.

Next, we determine if there are different classes of force-extension curves. We fit each curve with a family of polynomials with degrees ranging from 1 to 4 using a weighted least squares routine in Matlab (Mathworks). Weights are $w_i = 1/\delta f_i^2$ where δf_i is the measurement error on a data point. For each polynomial fit, a chi-square goodness-of-fit test was performed on the residuals to determine whether or not they followed a normal distribution (as would be the case if only noise remained in the signal after fitting). Curves were then categorized according to the smallest degree polynomial of the fit that returned residuals following a normal distribution. Force-extension relations that can be described by a polynomial of degree 1 or 2 are classified as "type I″ curves, shown in blue in Fig. 5. Cases requiring a higher order polynomial to eliminate structure in the residuals were further treated and classified according to the Chow test [Chow (1960)]. The Chow test rejects the null hypothesis that the data can be fit with a single set of regression coefficients. These cases were treated as follows. First the data was divided into subsets separated by break-points. A break-point could correspond to a single point defined by a spike in the residuals of the 2nd degree fit or it could be created by excluding a subset of data such as a bump or anomalously noisy region. The Chow test was then applied to the remaining data. In some cases, by excluding a subset of the data, a degree 1 or 2 polynomial could be fit to the remaining data (for example Fig. 5b, curve B– VI, Fig. 5c, curves C– I to C– V). These curves are classified as type I. In the remaining cases, the Chow test rejects the null hypothesis indicating the data is better fit with two different sets of regression coefficients. These are classified as "type II", shown in gold in Fig. 5. Applying the Chow test in this way lets us differentiate between curves with quadratic behaviour (expect for possibly a stand-alone spike) and curves requiring a more complex model to describe behaviour with kinks or discontinuities.

Fit parameters for the 2nd degree fits are shown in Fig. 7. For the coefficients of the quadratic model fit to each curve, the *t*-statistics and corresponding *p*-values were computed using a built-in Matlab routine. These statistics test the null hypothesis that a given coefficient is zero against the alternative hypothesis that it is nonzero. Less than 10 % of curves had a quadratic coefficient with a *t*-statistic with a *p*-value <0.05. The linear fit parameters for type I curves (all speeds) are distributed about a mean of 0.17 nN/μm with a SD of 0.12 nN/μm. According to the Mann-Whitney *U* test (MWU), this is a different distribution than that describing the linear parameters of type II curves, which has a mean of 0.28 nN/μm and a SD of 0.22 nN/μm. On the other hand, the MWU test shows that the quadratic parameters of type I and type II curves (all speeds) are drawn from the same distribution; we find the quadratic term to be -0.006 ± 0.011 nN/μm^2 for type I and -0.005 ± 0.022 nN/μm^2 for type II. Despite the large SD of the distribution, the quadratic term is statistically relevant. We discuss possible mechanisms for type I versus type II behaviour at the end of this section.

The same type I and type II behaviour emerges at different pull speeds (Fig. 7b–f). Surprisingly, we find the fit parameters to have the same scatter across all speeds investigated, as confirmed by the Kruskal-Wallis test. We observe the same behaviour with a 10-fold increase of extension rate. Thus rate-dependent mechanical effects (such as viscoelasticity) or active forces (due to a biologically 'active material' response) are small and statistically not detectable at these timescales.

The work to extend a neurite by 10 μm is 8.6±8.3 fJ (mean±SD) (Fig. 6). This result is consistent with previous studies [Lamoureux et al. (2002)]; find a value of 4 fJ to initially extend a single hippocampal neurite by 10 μm. However, we do not observe a positive linear relationship between extension rate and work to deform a neurite as reported for rat hippocampal neurons [Lamoureux et al. (2002)], the axons of embryonic chick sensory neurons [Zheng et al. (1991)], and the axons of rat ganglion neurons [Steketee et al. (2014)]. Our smallest elongation rate, 0.05 μm/s, is almost twice the largest extension rate reported for hippocampal neurites in towing experiments; put differently, we pull for much shorter timescales to achieve the same extension. We explore a different range of pull speeds and we find the behaviour of neurites under tension in this range is not modeled by a damping element (a Newtonian dashpot), unlike the behaviour of neurites at lower pull speeds [Mondaini and Pardalos (2008)]. We speculate that this is because at fast rates biologically 'active' forces are not relevant or measurable. Our measurements would thus be characteristic of the 'intrinsic' material properties. Indications of this are the observed cytoskeleton dynamics, which lag behind the mechanical pulling of neurites [Rigby et al. (2019)]. We also performed pulls at 37°C. While this dataset is too small to be statistically significant, we

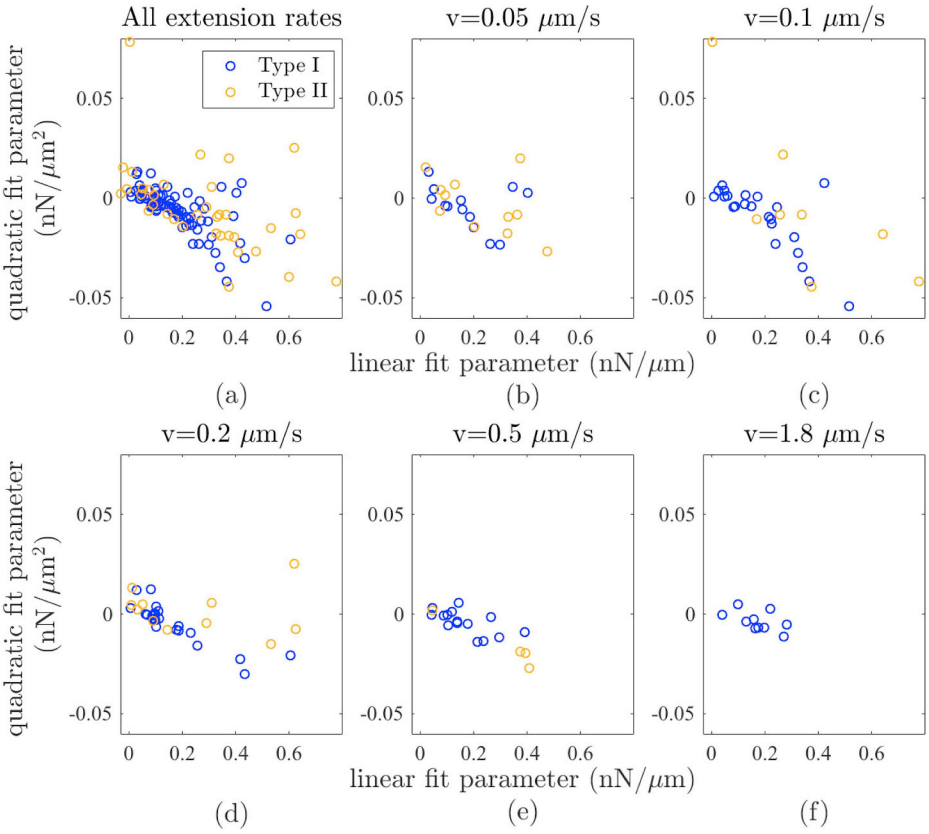

Fig. 7. Fit parameters for 2nd degree fits of type I (blue) and type II (gold) curves. **(a)** Quadratic fit parameter versus linear fit parameter for all pull speeds. The mean±SD for type I linear parameters is 0.17 ± 0.12 nN/μm and that of the quadratic parameter is − 0.006 ± 0.011 nN/μm^2. For type II curves the linear fit parameter is 0.28 nN/μm±0.22 nN/μm and the quadratic fit parameter is -0.005 ± 0.022 nN/μm^2 **(b–f)** Quadratic fit parameter versus linear fit parameter for each extension rate. We note the behaviour of the curves does not change, even with a 10-fold increase in the extension rate. The Kruskall-Wallis test is used to determine that the linear parameters at each pull speed are drawn from the same distribution, as are the quadratic fit parameters. (For interpretation of the references to colour in this figure legend, the reader is referred to the Web version of this article.)

note that values of stiffness constants obtained are within the lower bounds of the data in Fig. 7. This suggests temperature is not the dominant factor influencing the behaviour of the force-extension relations of neurites on timescales measured.

We conclude this section with a list of possible reasons for type I versus type II behaviour.

1 Axon versus dendrite: In our experiments, we do not know the nature of the pulled neurites (dendritic or axonal). It follows that type I versus type II behaviour could depend on the structure of the neurite. AFM experiments have shown stiffness of hippocampal axons to be larger than stiffness of dendrites under compression so it is reasonable that axonal and dendritic neurites respond differently to deformations under strain [Zhang et al. (2017)].
2 Multiple induced neurites: We sometimes observe that when a single bead is pulled away from a denditric structure, multiple neurites can be induced. Distinguishing the exact number of neurites is challenging due to the fact that their radii are often below the diffraction limit of our optical microscope. It is possible that one or more of these neurites could break off the bead during the pull leaving a discontinuity in the force-profile as in Fig. 8a&c. Experiments reported in [Magdesian et al. (2016)] point to bead-size as a factor influencing the number of neurites created and is an interesting avenue of future study.
3 Motion of submicron particles: Other possible reasons for type I versus type II behaviour are linked to the causes of bumps or spikes in the force-extension curves. In some cases, these jumps can be correlated to biological phenomena visible in the associated image series. For example, Fig. 5d, curves A− X, C− VI, C− VIII, have spikes associated with the motion of submicron particles along the neurite. An example is illustrated in Fig. 8b. These particles are likely organelles being transported along the neurite [Hurtig et al. (2010); Bressloff and Levien (2015); Suarez et al. (2013)] or membrane defects [Lobovkina et al. (2006)]. Our method quantifies these processes as variations in the force-extension profile (Fig. 8a).
4 Motion of neurite perpendicular to direction of pull: Bumps also occur in conjunction with the motion of neurites themselves in directions perpendicular to the motion of the beaded pipette tip, see Fig. 5b, curve A− II [Suarez et al. (2013)]. observed that after it had been stretched, a neurite would displace its initial point of contact along the axon, minimizing its length.

4. Conclusion

In this paper we have studied the mechanics of newly induced neurites; to our knowledge this is the only large-scale investigation of structures originating from parent axons or dendrites. We find that on timescales and distances probed, neurite extension is well described by a quadratic model with a stiffness constant of $1.7\times10^{-4}\pm1.2\times10^{-4}$ N/m and a quadratic term of -6 ± 11 N/m^2. The variation of this data

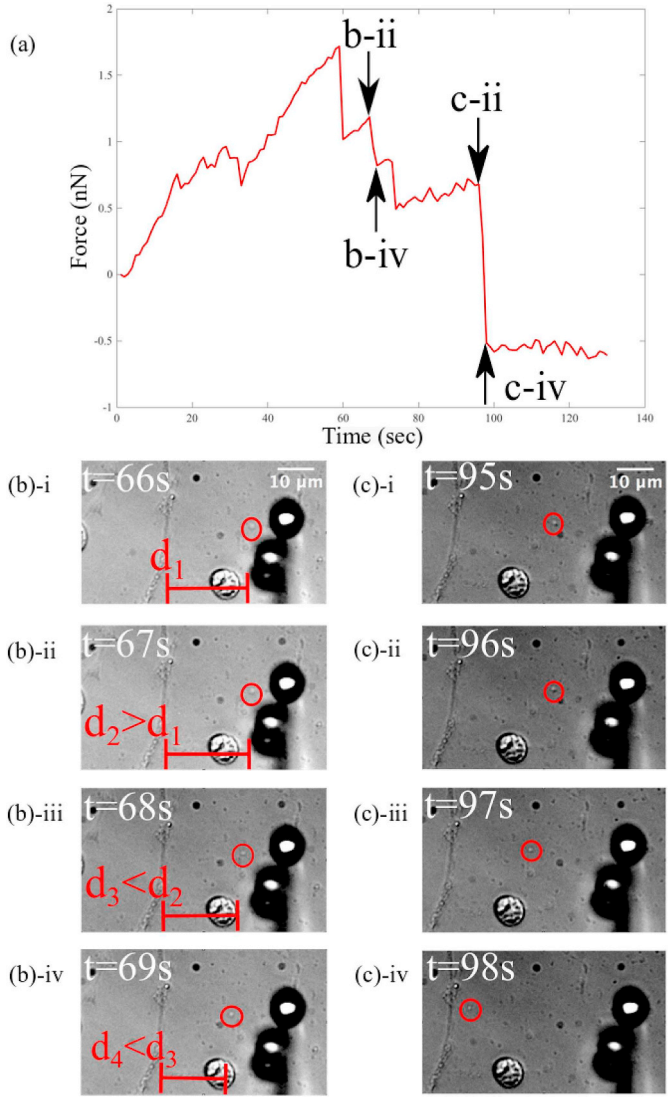

Fig. 8. Example of submicron particle-movement along a neurite corresponding to spikes in the force-profile. **(a)** Graph of force on the pipette-tip versus time; features that correspond to visible events in the image series are indicated with arrows. **(b)** Images at times corresponding to a bump in the force-time curve. From $t = 66$ s to $t = 67$ s, the distance between the submicron particle (red circles) and the neurite-initiation site increases (distances indicated with red scale bars). From $t = 67$ s to $t = 68$ s and again from $t = 68$ s to $t = 69$ s, the distance between the submicron particle and the neurite-initiation site decreases, even as the neurite-initiation site is pulled away from the bead. This decrease corresponds to a drop in force (b-ii-b-iv). **(c)** Images at times corresponding to the large drop in the force-time curve (c-i-c-iii). The neurite appears to break off the bead. This can be seen by the same submicron particle (circles) that jumps to the neurite-initiation site from $t = 96$ s to $t = 98$ s.

within a given pull speed is the same across all pull speeds, even with more than a 10-fold increase in speeds. For initial extensions of 10 μm we do not observe the linear relationship between work and pull speed previously reported for axons [Lamoureux et al. (2002); Zheng et al. (1991); Steketee et al. (2014)]. Finally, using statistically robust methods, we distinguish two types of behaviour characterized by either quadratic (type I) or discontinuous/non-monotonic (type II) force-extension relations, the latter being observed with a much lower frequency. In most cases, the continuous parts of the force-extension relationships of the type II curves have type I characteristics. Interestingly, the neurite-initiation site along the axis of the parent axon or dendrite did not influence our ability to initiate a neurite. This points to a uniformity in the branching potential of axons/dendrites.

To perform these studies, we have developed a multi-purpose system that combines flexible pipettes, functionalized beads and particle-tracking capabilities to enable robust, reproducible force measurements on individual cells. We show our system encompasses all the benefits of the traditional force sensing techniques with the added potential for more elaborate and/or higher-throughput experiments if the option of suction is used to attach beads to the pipette tip. The ability to release the beads means that multiple experiments can be performed. In our set-up, the pulled neurite is suspended in medium and does not contact the substrate unlike other, slower, methods of elongating axons that rely on chemical cues from a suitably compliant substrate, see e.g. [Kostic et al. (2007); Athamneh and Suter (2015)]. In these instances, as well as in works that use a combination of chemical and mechanical cues to explore the limits of neurite growth, cells are pulled along a substrate so the adhesion of the cell to the substrate can obscure the explicit roll of tension in the growth process [Bray (1984); Heidemann and Bray (2015)]. In fact, it is an open question how substrate stiffness affects axonal growth, electrophysiological and cytoskeleton function [Athamneh and Suter (2015); Athamneh et al. (2015)]. Tension applied to axons adhered to a deformable substrate leads to a disruption in the microtubule network [Tang-Schomer et al. (2010)] whereas tension applied to axons suspended in media (though at less extreme rates) leads to a normal cytoskeleton array and axons able to transmit active electrical signals [Heidemann and Bray (2015); Pfister et al. (2006, 2004)].

Future applications of the force probe could be to perform the same experiments described here on cell cultures treated with different cytoskeleton inhibitors to isolate the role of each cytoskeleton element in force generation and neurite initiation. This could connect our results to reports on the disruption of the cytoskeleton in response to applied tensile force [Ahmadzadeh et al. (2014); Tang-Schomer et al. (2010)]. Adjusting other experimental parameters such as the magnitudes and application times of applied strain, the adhesion of the neurite to a substrate and the elongation of an existing axon instead of a newly-created process could also give insights into the mechanisms governing developmental axon stretch versus those governing traumatic axon injury reported in [Loverde and Pfister (2015)]. Other applications are to combine electrophysiological techniques with our platform and explore various axonal injury models [Tian et al. (2019)].

Acknowledgements

The authors would like to acknowledge funding from the Natural Sciences and Engineering Research Council of Canada of Canada as well as from the Fonds de Recherche du Québec - Nature et Technologies, Regroupements stratégiques program. We thank Andrew Kaplan and Alyson Fournier for the gift of the lentiviruses.

Appendix A. Image acquisition.

The sample, which consisted of embryonic rat hippocampal neurons contained in a fluid cell, rested on the piezo-actuated stage of an MFP-3D-BIO AFM mounted on an inverted optical microscope (Olympus IX-71). The piezo stage allows nanometer-resolved positional control in the sample plane via custom MATLAB codes applied through a 16 bit converter (National Instruments, NI-6002) linked to the MFP-3D sample piezo scanner. Images of the sample, magnified by the 40×PH microscope objective with 0.6NA, were recorded by a charged-couple device (CCD) camera (Cascade II by Photometrics) attached to the sideport of the microscope that streams image stacks to a connected central processing unit (CPU). Bright-field imaging was used to track particles. Noise in the system arising from the building and acoustic vibrations was minimized by placing the entire set-up

on an active damping table (Herzan TS-Series) located within an acoustic insulation enclosure located on a passive optical table.

Images with resolutions of 512 × 512 pixels were acquired in our experiments at either 5.5 or 1 Hz rates with an exposure time of 75 m s. Our setup can achieve a temporal resolution of up to 20 Hz if the camera exposure time is adjusted and a smaller region of interest (ROI) is selected.

Appendix B. Image analysis.

The quality of the data was initially assessed with ImageJ. Factors considered included visibility of reference beads, whether or not the beaded probe tip eclipsed any other beads, and whether the pipette was raised sufficiently above the sample surface so as not to cause stick-slip events on the Petri dish surface. Videos were rejected after analysis if pulls were not significantly different from the corresponding null experiment. Images were analyzed in MATLAB (Mathworks) using a custom-made centroid tracking algorithm (which is available upon request) as described in [Cheezum et al. (2001)]. First, we manually isolate a bead from the initial field of view to a smaller region. As observed in the microscope, beads appear as dark semi-circles surrounding a high-intensity centre, the brightest spot on the image. Expressing each image as a matrix of intensities, $I(x, y)$, where x, y are the pixel coordinates, the centroid can be given in terms of the moment, M_{ij}, of an image, defined as

$$M_{ij} = \sum_{x=1}^{L_x} \sum_{y=1}^{L_y} x^i y^j I(x, y). \tag{B.1}$$

In the above, the L_n are the respective dimension lengths in pixels. The image centroid is

$$(x_C, y_C) = \left(\frac{M_{10}}{M_{00}}, \frac{M_{01}}{M_{00}} \right). \tag{B.2}$$

Note that in Equations (B.1) and (B.2), a threshold has been applied such that all pixels in I corresponding to intensities below said threshold are assigned a zero value, ensuring only the brightest region of the image is tracked. Detecting and comparing the centroid of a particle in two successive images indicates the distance an object has travelled.

References

Ahmadzadeh, H., Smith, D.H., Shenoy, V.B., 2014. Viscoelasticity of tau proteins leads to strain rate-dependent breaking of microtubules during axonal stretch injury: predictions from a mathematical model. Biophys. J. 106 (5), 1123–1133.

Alexander, B.F., Ng, K.C., 1991. Elimination of systematic error in subpixel accuracy centroid estimation. [also letter 34 (11) 3347-3348 (nov1995)]. Opt. Eng. 30 (9), 1320–1332.

Ares, J., Arines, J., 2004. Influence of thresholding on centroid statistics: full analytical description. Appl. Optic. 43 (31), 5796–5805.

Athamneh, A.I., Cartagena-Rivera, A.X., Raman, A., Suter, D.M., 2015. Substrate deformation predicts neuronal growth cone advance. Biophys. J. 109 (7), 1358–1371.

Athamneh, A.I.M., Suter, D.M., 2015. Quantifying mechanical force in axonal growth and guidance. Front. Cell. Neurosci. 9, 359.

Bernal, R., Pullarkat, P.A., Melo, F., 2007. Mechanical properties of axons. Phys. Rev. Lett. 99 (1), 018301.

Bray, D., 1984. Axonal growth in response to experimentally applied mechanical tension. Dev. Biol. 102 (2), 379–389.

Bressloff, P.C., Levien, E., 2015. Synaptic democracy and vesicular transport in axons. Phys. Rev. Lett. 114 (16), 168101.

Cheezum, M.K., Walker, W.F., Guilford, W.H., 2001. Quantitative comparison of algorithms for tracking single fluorescent particles. Biophys. J. 81 (4), 2378–2388.

Chow, G.C., 1960. Tests of equality between sets of coefficients in two linear regressions. Econometrica: J. Econom. Soc. 591–605.

Dai, J., Sheetz, M.P., Wan, X., Morris, C.E., 1998. Membrane tension in swelling and shrinking molluscan neurons. J. Neurosci. 18 (17), 6681–6692.

Dennerll, T.J., Lamoureux, P., Buxbaum, R.E., Heidemann, S.R., 1989. The cytomechanics of axonal elongation and retraction. J. Cell Biol. 109 (6), 3073–3083.

Dotti, C.G., Sullivan, C.A., Banker, G.A., 1988. The establishment of polarity by hippocampal neurons in culture. J. Neurosci. 8 (4), 1454–1468.

Franze, K., Gerdelmann, J., Weick, M., Betz, T., Pawlizak, S., Lakadamyali, M., Bayer, J., Rillich, K., Gögler, M., Lu, Y.-B., et al., 2009. Neurite branch retraction is caused by a threshold-dependent mechanical impact. Biophys. J. 97 (7), 1883–1890.

Fuhs, T., Reuter, L., Vonderhaid, I., Claudepierre, T., Käs, J.A., 2013. Inherently slow and weak forward forces of neuronal growth cones measured by a drift-stabilized atomic force microscope. Cytoskeleton 70 (1), 44–53.

Heidemann, S.R., Bray, D., 2015. Tension-driven axon assembly: a possible mechanism. Front. Cell. Neurosci. 9, 316.

Hochmuth, F., Shao, J.-Y., Dai, J., Sheetz, M.P., 1996. Deformation and flow of membrane into tethers extracted from neuronal growth cones. Biophys. J. 70 (1), 358–369.

Hurtig, J., Chiu, D.T., Önfelt, B., 2010. Intercellular nanotubes: insights from imaging studies and beyond. Wiley Interdiscip. Rev.: Nanomed. Nanobiotechnol. 2 (3), 260–276.

Hutter, J.L., 2005. Comment on tilt of atomic force microscope cantilevers: effect on spring constant and adhesion measurements. Langmuir 21 (6), 2630–2632.

Hutter, J.L., Bechhoefer, J., 1993. Calibration of atomic-force microscope tips. Rev. Sci. Instrum. 64 (7), 1868–1873.

Kaplan, A., Morquette, B., Kroner, A., Leong, S., Madwar, C., Sanz, R., Banerjee, S.L., Antel, J., Bisson, N., David, S., et al., 2017. Small-molecule stabilization of 14-3-3 protein-protein interactions stimulates axon regeneration. Neuron 93 (5), 1082–1093.

Karhu, E., Gooyers, M., Hutter, J.L., 2009. Quantitative friction-force measurements by longitudinal atomic force microscope imaging. Langmuir 25 (11), 6203–6213.

Kostic, A., Sap, J., Sheetz, M.P., 2007. Rptpα is required for rigidity-dependent inhibition of extension and differentiation of hippocampal neurons. J. Cell Sci. 120 (21), 3895–3904.

Lamoureux, P., Ruthel, G., Buxbaum, R.E., Heidemann, S.R., 2002. Mechanical tension can specify axonal fate in hippocampal neurons. J. Cell Biol. 159 (3), 499–508.

Lobovkina, T., Dommersnes, P., Joanny, J.-F., Hurtig, J., Orwar, O., 2006. Zipper dynamics of surfactant nanotube y junctions. Phys. Rev. Lett. 97 (18), 188105.

Loverde, J.R., Pfister, B.J., 2015. Developmental axon stretch stimulates neuron growth while maintaining normal electrical activity, intracellular calcium flux, and somatic morphology. Front. Cell. Neurosci. 9, 308.

Lucido, A.L., Sanchez, F.S., Thostrup, P., Kwiatkowski, A.V., Leal-Ortiz, S., Gopalakrishnan, G., Liazoghli, D., Belkaid, W., Lennox, R.B., Grutter, P., et al., 2009. Rapid assembly of functional presynaptic boutons triggered by adhesive contacts. J. Neurosci. 29 (40), 12449–12466.

Magdesian, M.H., Anthonisen, M., Lopez-Ayon, G.M., Chua, X.Y., Rigby, M., Grütter, P., 2017. Rewiring neuronal circuits: a new method for fast neurite extension and functional neuronal connection. J. Vis. Exp.(124), e55697.

Magdesian, M.H., Lopez-Ayon, G.M., Mori, M., Boudreau, D., Goulet-Hanssens, A., Sanz, R., Miyahara, Y., Barrett, C.J., Fournier, A.E., De Koninck, Y., et al., 2016. Rapid mechanically controlled rewiring of neuronal circuits. J. Neurosci. 36 (3), 979–987.

Mondaini, R.P., Pardalos, P.M., 2008. Mathematical Modelling of Biosystems, vol. 102 Springer Science & Business Media.

O'Toole, M., Lamoureux, P., Miller, K.E., 2008. A physical model of axonal elongation: force, viscosity, and adhesions govern the mode of outgrowth. Biophys. J. 94 (7), 2610–2620.

Pfister, B.J., Bonislawski, D.P., Smith, D.H., Cohen, A.S., 2006. Stretch-grown axons retain the ability to transmit active electrical signals. FEBS Lett. 580 (14), 3525–3531.

Pfister, B.J., Iwata, A., Meaney, D.F., Smith, D.H., 2004. Extreme stretch growth of integrated axons. J. Neurosci. 24 (36), 7978–7983.

Rigby, M., Anthonisen, M., Chua, X.Y., Kaplan, A., Fournier, A., Grutter, P., January 2019. Building an Artificial Neural Network with Neurons. submitted for publication.

Sánchez, F.S., 2011. AFM Investigations of Cellular Response to Environmental and Local Chemo-Mechanical Stimulus. McGill University (Canada).

Shimamoto, Y., Kapoor, T.M., 2012. Microneedle-based analysis of the micromechanics of the metaphase spindle assembled in xenopus laevis egg extracts. Nat. Protoc. 7 (5), 959.

Steketee, M.B., Oboudiyat, C., Daneman, R., Trakhtenberg, E., Lamoureux, P., Weinstein, J.E., Heidemann, S., Barres, B.A., Goldberg, J.L., 2014. Regulation of intrinsic axon growth ability at retinal ganglion cell growth cones. Investig. Ophthalmol. Vis. Sci. 55 (7), 4369–4377.

Suarez, F., Thostrup, P., Colman, D., Grutter, P., 2013. Dynamics of presynaptic protein recruitment induced by local presentation of artificial adhesive contacts. Dev.

Neurobiol. 73 (1), 98–106.
Tang-Schomer, M.D., Patel, A.R., Baas, P.W., Smith, D.H., 2010. Mechanical breaking of microtubules in axons during dynamic stretch injury underlies delayed elasticity, microtubule disassembly, and axon degeneration. FASEB J. 24 (5), 1401–1410.
Tian, J., Huang, G., Lin, M., Qiu, J., Sha, B., Lu, T.J., Xu, F., 2019. A mechanoelectrical coupling model of neurons under stretching. J. Mech. Behav. Biomed. Mater. 93, 213–221.
Waxman, S.G., Kocsis, J.D., Stys, P.K., 1995. The Axon: Structure, Function, and Pathophysiology. Oxford University Press, USA.
Zhang, Y., Abiraman, K., Li, H., Pierce, D.M., Tzingounis, A.V., Lykotrafitis, G., 2017. Modeling of the axon membrane skeleton structure and implications for its mechanical properties. PLoS Comput. Biol. 13 (2), e1005407.
Zhang, Z., Menq, C.-H., 2008. Three-dimensional particle tracking with subnanometer resolution using off-focus images. Appl. Optic. 47 (13), 2361–2370.
Zheng, J., Lamoureux, P., Santiago, V., Dennerll, T., Buxbaum, R.E., Heidemann, S.R., 1991. Tensile regulation of axonal elongation and initiation. J. Neurosci. 11 (4), 1117–1125.